Semi-Blind Ultrasound Image Deconvolution from Compressed Measurements

Z. Chen [a,*], A. Basarab [b], D. Kouamé [b]

[a] *Institute of Sensors, Signals and Systems, Heriot-Watt University, EH14 4AS, UK*
[b] *University of Toulouse, IRIT, UMR CNRS 5505, Toulouse, France*

Highlights

- Estimating the PSF at the same time in the recently proposed compressive deconvolution framework for ultrasound imaging.
- Taking fully advantage of the existing method of PSF estimation.
- Presenting an analytical solution to the sub-problem of PSF.

Graphical abstract

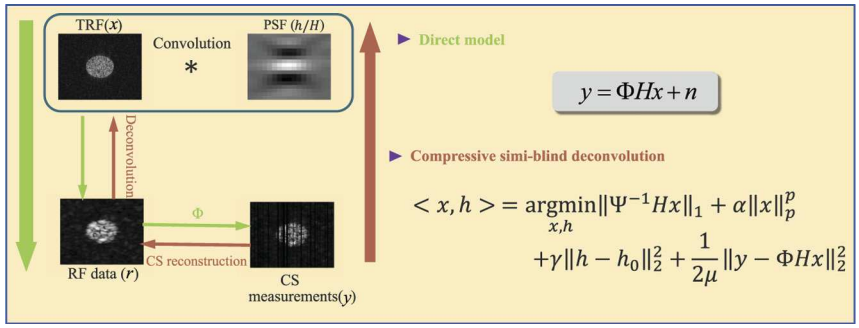

Abstract

The recently proposed framework of ultrasound compressive deconvolution offers the possibility of decreasing the acquired data while improving the image spatial resolution. By combining compressive sampling and image deconvolution, the direct model of compressive deconvolution combines random projections and 2D convolution with a spatially invariant point spread function. Considering the point spread function known, existing algorithms have shown the ability of this framework to reconstruct enhanced ultrasound images from compressed measurements by inverting the forward linear model. In this paper, we propose an extension of the previous approach for compressive blind deconvolution, whose aim is to jointly estimate the ultrasound image and the system point spread function. The performance of the method is evaluated on both simulated and *in vivo* ultrasound data.

Keywords: Ultrasound imaging; Compressive sampling; Blind deconvolution

1. Introduction

Despite its intrinsic rapidity of acquisition, several ultrasound (US) applications such as duplex Doppler or 3D imaging may require higher frame rates than those provided by conventional acquisition schemes or may suffer from the high amount of acquired data. In this context, compressive sampling (CS) framework appears as an appealing solution to overcome these issues. Since the first works in compressive US imaging published in 2010 [1–4], there have been several studies devoted to this topic to date [5–11]. Conventional approach to sample sig-

* Corresponding author.
E-mail address: zhouye.chen@hw.ac.uk (Z. Chen).

https://doi.org/10.1016/j.irbm.2017.11.002

nals or images follows the Shannon–Nyquist theorem. According to the Shannon–Nyquist sampling theorem, the sampling rate must be at least twice the maximum frequency contained by the signal. However, the theory of CS makes it possible to go against the common knowledge in data acquisition. It allows to recover, via non linear optimization routines, an image from few linear measurements (below the limit standardly imposed by the Shannon–Nyquist theorem) provided two conditions: i) the image must be sparse in a known basis or frame and ii) the measurement matrix must be incoherent with the sparsifying basis [12]. Existing works focused on these two aspects, *i.e.* the sparsity study and the incoherent acquisition, have shown that it is possible to recover US radio-frequency (RF) images based on their sparsity in basis such as 2D Fourier transform [13], wavelets [14], waveatoms [15], or learning dictionaries [6], using various acquisition schemes such as projections on Gaussian [4] or Bernoulli random vectors [13], plane-wave emissions [14] or Xampling [5].

However, despite the promising results, there are still two remaining problems regarding the application of CS in US imaging. i) Since perfect sparsity is almost never reachable due to the presence of noise and the incoherence between measurement matrix and sparse basis cannot be easily satisfied in practical situations, the images reconstructed from compressed measurements tend to be less good compared to standard acquisitions, especially for a low number of measurements. ii) In the case where an exact CS recovery is possible, *i.e.*, the quality in terms of resolution of the recovered US images is equivalent to those acquired using standard schemes, whereas it is widely accepted that image quality is one of the open challenges in US imaging. The signal-to-noise ratio, the spatial resolution and the contrast of standard US images are affected by the physical phenomenons related to US wave propagation and limited by the bandwidth of the transducer of imaging system.

Image deconvolution represents a valuable tool that can be used for improving image quality without requiring complicated calibrations of the real-time image acquisition and processing systems. US image deconvolution has been extensively studied in the literature, showing very promising results [16–18]. Motivated by the interest of CS and deconvolution, we have recently proposed a framework called compressive deconvolution (CD) in US imaging [19]. The objective was to reconstruct enhanced RF images from compressed linear measurements, aiming to obtain a higher frame rate or less data volume and to enhance the image contrast at the same time. The main idea behind CD is to combine CS and deconvolution, leading to the following linear direct model:

$$\boldsymbol{y} = \Phi H \boldsymbol{x} + \boldsymbol{n} \tag{1}$$

where $\boldsymbol{y} \in \mathbb{R}^M$ stands for the M linear compressed measurements obtained for one RF image $H\boldsymbol{x}$ and $\Phi \in \mathbb{R}^{M \times N}$ ($M << N$) corresponds to the CS acquisition matrix. The RF image $H\boldsymbol{x}$ models that the tissue reflectivity function (TRF) $\boldsymbol{x} \in \mathbb{R}^N$ is degraded by $H \in \mathbb{R}^{N \times N}$, which is a block circulant with circulant block (BCCB) matrix related to the 2D PSF of the US system. Finally, $\boldsymbol{n} \in \mathbb{R}^M$ represents a zero-mean additive white Gaussian noise. We emphasize that all the images in (1) are expressed in the standard lexicographical order.

Inverting the model in (1) will allow us to estimate the TRF $\boldsymbol{x}$, which is considered as a higher resolved US image, from the compressed RF measurements $\boldsymbol{y}$. Though similar models have been recently proposed for general image processing purpose [20–23] including a theoretical derivation of RIP for random mask imaging [24], we formulated in [19] the reconstruction process into a constrained optimization problem exploiting the relationship between CS recovery and deconvolution:

$$\begin{aligned} \underset{\boldsymbol{x}\in\mathbb{R}^N, \boldsymbol{a}\in\mathbb{R}^N}{min} & \parallel \boldsymbol{a} \parallel_1 + \alpha \| \boldsymbol{x} \|_p^p + \frac{1}{2\mu} \parallel \boldsymbol{y} - \Phi\Psi\boldsymbol{a} \parallel_2^2 \\ s.t. \quad & H\boldsymbol{x} = \Psi\boldsymbol{a} \end{aligned} \tag{2}$$

where $\boldsymbol{a}$ is the sparse representation of the US RF image $H\boldsymbol{x}$ in the transformed domain Ψ. It enables the reconstruction of the RF image and the TRF at the same time. α and μ are hyperparameters balancing the weight of each term in the cost function to minimize. The optimization problem above includes three terms: i) the ℓ_1-norm term aiming at imposing the sparsity of the RF image in the sparse basis Ψ, ii) the ℓ_p-norm term modeling the *a priori* of the target image $\boldsymbol{x}$, where the shape parameter p related to the Generalized Gaussian Distribution (GGD) is ranging from 1 to 2 ($1 \leq p \leq 2$), allowing us to generalize the existing works in US image deconvolution mainly based on Laplacian or Gaussian statistics [25,26], iii) the data fidelity term.

In order to solve this problem, an algorithm based on the Alternative Direction Method of Multipliers (ADMM) was initially proposed in [19] and was further improved with faster convergence based on Simultaneous Direction Method of Multipliers (SDMM) in [27]. Both algorithms have achieved promising results with the assumption that the PSF was known or could be estimated in a pre-processing step. However, the PSF cannot be perfectly known in practical situations. An initial investigation to jointly estimate the PSF has been recently published in [28] to show the possibility of recovering RF image, TRF and PSF at the same time.

In this paper, following the previous work and exploiting the prior information on the PSF, we propose and detail a compressive semi-blind deconvolution (CSBD) algorithm. The results on simulated and experimental images show improved performance compared to the non-blind approach. The remainder of this paper is organized as follows. In Section 2 we formulate the compressive semi-blind deconvolution problem. Section 3 details our proposed CSBD algorithm and simulation results are shown in Section 4 before drawing the conclusions in Section 5.

2. Methods

2.1. Problem formulation

Given the commutativity of the 2D convolution product, let us write the CD direct model in a different form, that includes the PSF kernel $\boldsymbol{h}$ instead of the associated BCCB matrix H:

$$\boldsymbol{y} = \Phi X P \boldsymbol{h} + \boldsymbol{n} \tag{3}$$

where $X \in \mathbb{R}^{N\times N}$ is a Block Circulant with Circulant Block (BCCB) matrix with the same structure as H, with the circulant kernel $\boldsymbol{x} \in \mathbb{R}^N$. $\boldsymbol{h} \in \mathbb{R}^n$ represents the PSF with a support of size n. $P \in \mathbb{R}^{N\times n}$ is a simple structure matrix mapping the n coefficients of the PSF kernel $\boldsymbol{h}$ to a N length vector so that $H\boldsymbol{x} = XP\boldsymbol{h}$. Its definition and implementation details can be found in Appendix A.

Inspired by the existing joint identification methods for blind deconvolution problem [26,29,30] and the prior information about the PSF such as the sampling frequency of the system, we formulate the compressive semi-blind deconvolution problem as below.

$$\begin{aligned} \min_{\boldsymbol{x}\in\mathbb{R}^N,\boldsymbol{a}\in\mathbb{R}^N,\boldsymbol{h}\in\mathbb{R}^s} & \parallel \boldsymbol{a} \parallel_1 + \alpha\parallel \boldsymbol{x}\parallel_p^p + \gamma \parallel \boldsymbol{h} - \boldsymbol{h}_0 \parallel_2^2 \\ & + \frac{1}{2\mu} \parallel \boldsymbol{y} - \Phi\Psi\boldsymbol{a} \parallel_2^2 \\ s.t. \quad & H\boldsymbol{x} = \Psi\boldsymbol{a} \end{aligned} \tag{4}$$

where $\boldsymbol{h}_0$ represents an initial guess of the PSF and γ is a positive hyper-parameter. The objective function in (4) contains, in addition to the three terms that we detailed in the introduction, a regularization term for the PSF. Similar to [31,32], we hereby incorporated the a *priori* on the PSF as a fidelity-type term.

Compared to the objective function of the non-blind CD problem in (2), we face herein a non-convex optimization problem. In order to solve this non-convex problem, we propose hereafter a dedicated alternate algorithm.

2.2. Proposed algorithm

Though the aforementioned cost function is non-convex, it is in fact strictly convex with respect to variables $\boldsymbol{x}$, $\boldsymbol{a}$ and $\boldsymbol{h}$ respectively. Based on the alternating minimization scheme [33] and CD algorithms in [19,27], we divide the problem in (4) into two sub-problems.

$$\begin{cases} (\boldsymbol{x}^{k+1}, \boldsymbol{a}^{k+1}) = \underset{\boldsymbol{x}\in\mathbb{R}^N,\boldsymbol{a}\in\mathbb{R}^N}{argmin} \parallel \boldsymbol{a} \parallel_1 + \alpha\parallel \boldsymbol{x}\parallel_p^p \\ \quad + \frac{1}{2\mu} \parallel \boldsymbol{y} - \Phi\Psi\boldsymbol{a} \parallel_2^2 \quad s.t. \quad H^k\boldsymbol{x} = \Psi\boldsymbol{a} \\ \boldsymbol{h}^{k+1} = \underset{\boldsymbol{h}\in\mathbb{R}^n}{argmin} \quad \gamma \parallel \boldsymbol{h} - \boldsymbol{h}_0 \parallel_2^2 \quad s.t. \quad X^{k+1}P\boldsymbol{h} = \Psi\boldsymbol{a}^{k+1} \end{cases} \tag{5}$$

where k is the iteration index. The first sub-problem which aims at estimating $\boldsymbol{a}$ and $\boldsymbol{x}$ for a fixed $\boldsymbol{h}$ at kth iteration is in fact the same with the CD problem addressed in [19,27]. Both the ADMM-based and SDMM-based algorithms are able to estimate $\boldsymbol{x}^{k+1}$ and $\boldsymbol{a}^{k+1}$ at the same time. The details of SDMM-based algorithm that we use herein can be found in Algorithm 1.

The second sub-problem can be solved by reformulating it in an unconstrained form

$$\boldsymbol{h}^{k+1} = \underset{\boldsymbol{h}\in\mathbb{R}^n}{argmin} \quad \gamma \parallel \boldsymbol{h} - \boldsymbol{h}_0 \parallel_2^2 + \parallel X^{k+1}P\boldsymbol{h} - \Psi\boldsymbol{a}^{k+1} \parallel_2^2 \tag{6}$$

It thus becomes a regularized least square problem and the corresponding analytical solution is

Algorithm 1 Compressive deconvolution SDMM-based algorithm.

Require: $C_1 = \Psi^{-1}H$, $C_2 = I_N$, $C_3 = H$, α, μ, β, $\boldsymbol{v}_i^0$, $\boldsymbol{b}_i^0$, $i = 1,2,3$

while not converged **do**

$\boldsymbol{x}^{j+1} \leftarrow \underset{\boldsymbol{x}}{argmin} \frac{1}{2\beta}\sum_i^3 \parallel \boldsymbol{b}^j - C_i\boldsymbol{x} - \boldsymbol{v}^j \parallel_2^2$

$\boldsymbol{v}_1^{j+1} \leftarrow \underset{\boldsymbol{v}_1}{argmin} \parallel \boldsymbol{v}_1 \parallel + \frac{1}{2\beta}\parallel \boldsymbol{b}_1^j - C_1\boldsymbol{x}^{j+1} - \boldsymbol{v}_1^j \parallel_2^2$

$\boldsymbol{v}_2^{j+1} \leftarrow \underset{\boldsymbol{v}_2}{argmin} \alpha\parallel \boldsymbol{v}_2 \parallel_p^p + \frac{1}{2\beta}\parallel \boldsymbol{b}_2^j - C_2\boldsymbol{x}^{j+1} - \boldsymbol{v}_2^j \parallel_2^2$

$\boldsymbol{v}_3^{j+1} \leftarrow \underset{\boldsymbol{v}_3}{argmin} \frac{1}{2\mu}\parallel \boldsymbol{y} - \Phi C_3\boldsymbol{v}_3 \parallel + \frac{1}{2\beta}\parallel \boldsymbol{b}_3^j - C_3\boldsymbol{x}^{j+1} - \boldsymbol{v}_3^j \parallel_2^2$

$\boldsymbol{b}_i^{j+1} = \boldsymbol{b}_i^j + C_i\boldsymbol{x}^{j+1} - \boldsymbol{v}_i^{j+1}$, $j = 1,2,3$

end while

Ensure: $\boldsymbol{x}, \boldsymbol{a} = \boldsymbol{v}_1$

$$\boldsymbol{h}^{k+1} = [(X^{k+1}P)^t X^{k+1}P + \gamma I_n]^{-1}[(X^{k+1}P)^t \Psi\boldsymbol{a}^{k+1} + \gamma\boldsymbol{h}_0] \tag{7}$$

where $I_n \in \mathbb{R}^n$ is the identity matrix. Based on the model reformulation in (3), the analytical solution for estimating the PSF only requires the inversion of an $n \times n$ (the size of the PSF kernel) matrix instead of an $N \times N$ (the size of the TRF) matrix. The computational cost is thus considerably reduced. More details about the practical implementation of the analytic solution in (7) can be found in Appendix B.

The proposed CSBD algorithm is summarized in Algorithm 2.

Algorithm 2 Compressive semi-blind deconvolution algorithm.

Input: $\boldsymbol{h}_0$, α, μ, β, γ

while not converged **do**

$\boldsymbol{x}^{k+1}, \boldsymbol{a}^{k+1} \leftarrow \boldsymbol{h}^k$ ▷ update $\boldsymbol{x}^{k+1}$, $\boldsymbol{a}^{k+1}$ using Algorithm 1

$\boldsymbol{h}^{k+1} \leftarrow \boldsymbol{x}^{k+1}, \boldsymbol{a}^{k+1}$ ▷ update $\boldsymbol{h}^{k+1}$ using (7)

end while

Output: $\boldsymbol{x}, \boldsymbol{a}, \boldsymbol{h}$

3. Results

In this section, the performance of the proposed compressive semi-blind deconvolution method are evaluated on both simulated and experimental data sets.

3.1. Simulated US data

To get a quantitative insight about the algorithm performance, we first address the restoration of TRF, RF image and PSF on simulated US data where the degradation process (e.g., the variance of the additive Gaussian noise and the PSF) is known. To be in consistent with the direct model and regularizations we proposed in this paper, we simulated the envelope US image with a 2D convolution between the TRF and a 7×7 spatially invariant Gaussian PSF of variance 2. The TRF sized of 300×300 was generated by assigning the scatterers random amplitudes following a given distribution, weighted by a cartoon image named by mask hereafter. A Laplacian distribution has been employed and the mask has been hand drawn to simulate four different regions with different echogenicities. The resulting TRF and US image (plotted in B-mode) are shown in Fig. 1(a) and (b), respectively. The compressed measurements

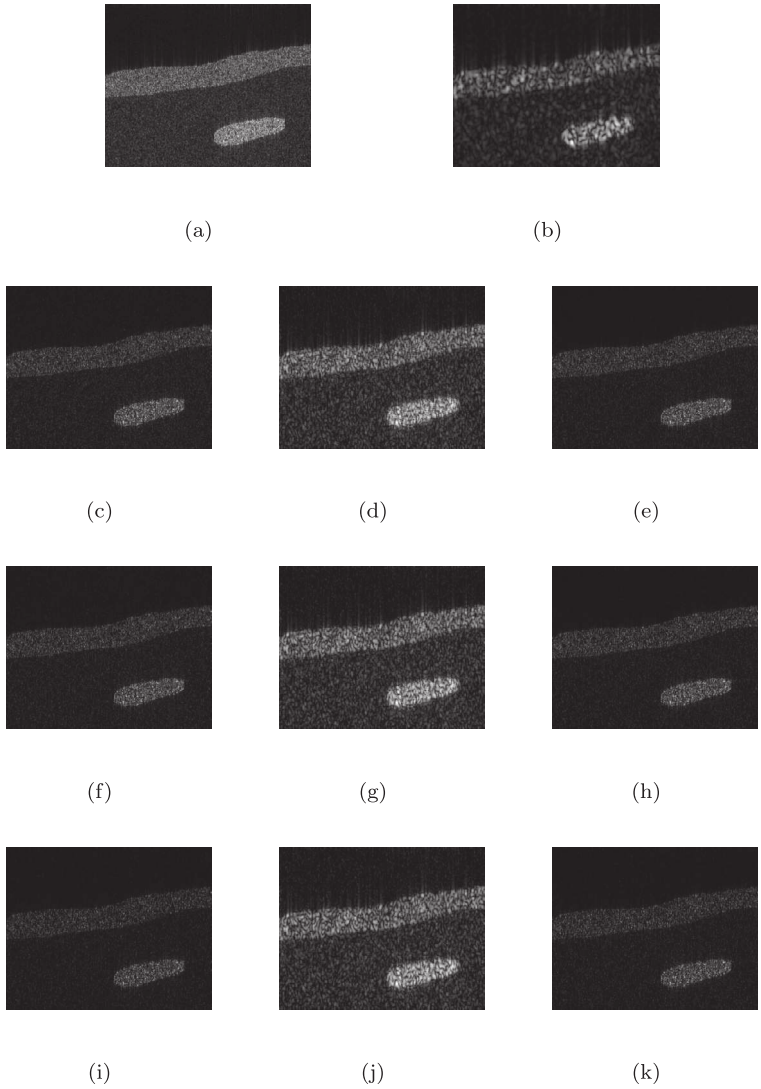

Fig. 1. Simulated US image and its compressive blind deconvolution results for a SNR of 40 dB. (a) Original tissue reflectivity function, (b) simulated B-mode US image, (c), (f), (i) results using CD with the true PSF for CS ratios of 0.8, 0.6 and 0.4, (d), (g), (j) results using CD with a pre-estimated PSF for CS ratios of 0.8, 0.6 and 0.4, (e), (h), (k) results using CSBD for CS ratios of 0.8, 0.6 and 0.4.

were obtained by projecting the US images onto an orthogonal structurally random matrix (SRM) [34] and were degraded by an additive Gaussian noise corresponding to an SNR of 40 dB.

Based on the simulated US image in Fig. 1(b), an initial guess of the PSF was estimated using the algorithm in [16], shown in Fig. 2(b). Fig. 1(c)–(k) show a series of TRF reconstruction results using the SDMM-based CD algorithm given in Algorithm 1 with the known PSF, the SDMM-based CD with the initial estimated PSF and the proposed CSBD approach for CS ratios running from 0.4 to 0.8. We have also displayed the estimated PSFs in Fig. 2(c)–(e).

To evaluate the results quantitatively, we hereby employed two metrics: the standard peak signal-to-noise ratio (PSNR) and the Structural Similarity (SSIM) [35].

PSNR is defined as

$$PSNR = 10log_{10}\frac{NL^2}{\| \boldsymbol{x} - \hat{\boldsymbol{x}} \|^2} \tag{8}$$

where $\boldsymbol{x}$ and $\hat{\boldsymbol{x}}$ are the original and reconstructed images, N stands for the number of pixels in the image and the constant L represents the maximum intensity value in $\boldsymbol{x}$.

SSIM, extensively used in US imaging, is defined as

$$SSIM = \frac{(2\mu_x\mu_{\hat{x}} + c_1)(2\sigma_{x\hat{x}} + c_2)}{(\mu_x^2 + \mu_{\hat{x}}^2 + c_1)(\sigma_x^2 + \sigma_{\hat{x}}^2 + c_2)} \tag{9}$$

where x and $\hat{x}$ are the original and reconstructed images, μ_x, $\mu_{\hat{x}}$, σ_x and $\sigma_{\hat{x}}$ are the mean and variance values of x and $\hat{x}$, $\sigma_{x\hat{x}}$ is the covariance between x and $\hat{x}$; $c_1 = (k_1L)^2$ and $c_2 = (k_2L)^2$ are two variables aiming at stabilizing the division with weak denominator, L is the dynamic range of the pixel-values and k_1, k_2 are constants. In this paper, L was set to 1, k_1 to 0.01 and k_2 to 0.03.

Table 1 regroups the PSNRs obtained with the proposed method, with SDMM-based CD algorithms using the known PSF (denoted as CD_true) and with SDMM-based CD algo-

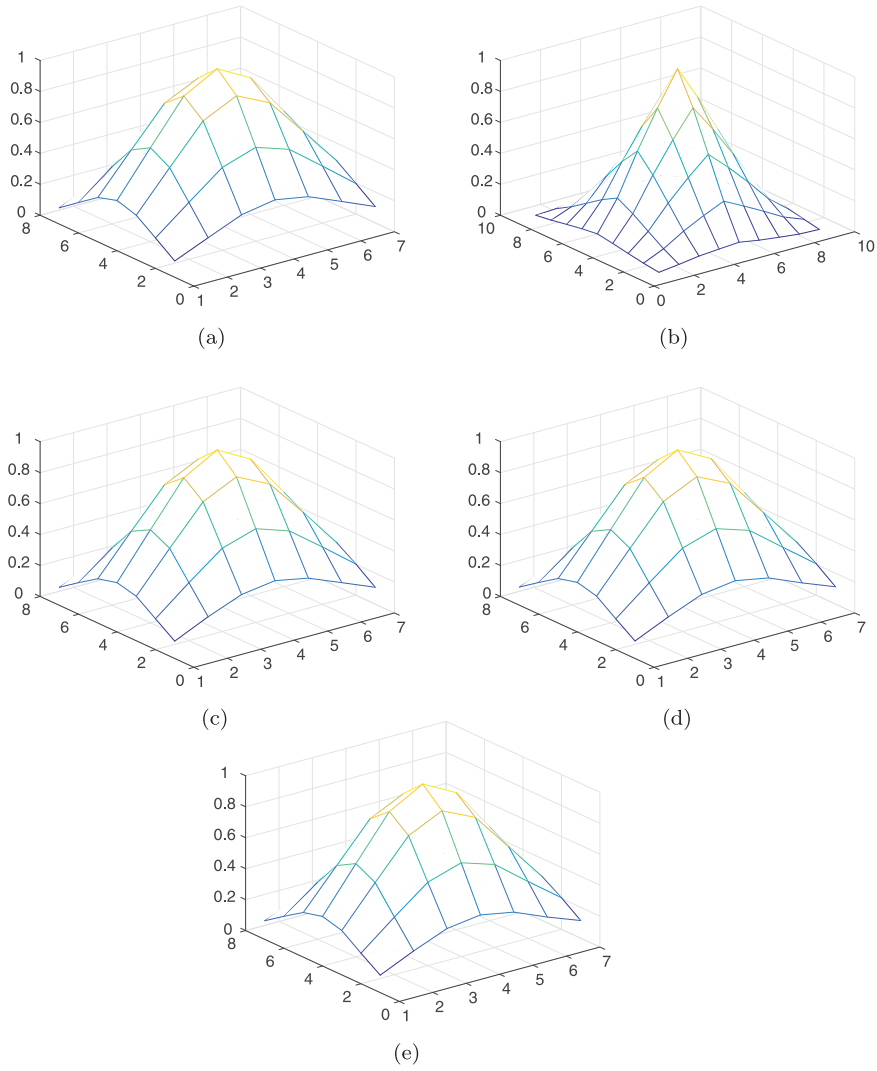

Fig. 2. Estimated PSFs of CSBD. (a) True PSF, (b) estimated PSF using an existing method [16], (c), (d), (e) estimated PSF of CSBD for CS ratios of 0.8, 0.6 and 0.4.

Table 1
Quantitative assessment for simulated US data.

Methods	CS ratios	PSNRx	SSIM	PSNRh
CD_true	80%	29.29	80.10	–
	60%	28.57	78.14	
	40%	27.07	73.91	
	20%	25.29	61.07	
CD	80%	22.32	52.04	21.36
	60%	22.33	50.51	
	40%	22.49	49.66	
	20%	22.72	45.76	
CSBD	80%	28.55	80.03	44.74
	60%	27.31	77.35	45.24
	40%	26.87	73.22	44.68
	20%	25.01	58.36	41.59

rithms using the initially estimated PSF for four CS ratios from 0.2 to 0.8. In each case, the reported PSNRs are the mean values of 10 experiments.

3.2. *In vivo US data*

In this section, we tested our proposed method with an *in vivo* image. The image (sized by 250 × 180) shown in Fig. 3(a) was acquired with a 20 MHz single-element US probe and corresponds to part of a mouse kidney. In order to fit the compressive deconvolution framework, the measurements with CS ratios of 0.8, 0.6 and 0.4 were obtained by projecting the RF image onto the SRM and by further degradation with an additive Gaussian noise corresponding to an SNR of 40 dB. Similar to the simulation results, the initial PSF in Fig. 4 was estimated from the data using the method presented in [16]. Fig. 3 displays the TRF reconstruction results of the proposed method and Fig. 4 presents the corresponding PSFs.

3.3. *Results' discussion*

We may firstly remark from the results on the simulated data in Fig. 1 and the quantitative metrics in Table 1 that the proposed CSBD ourperforms the non-blind CD method with an

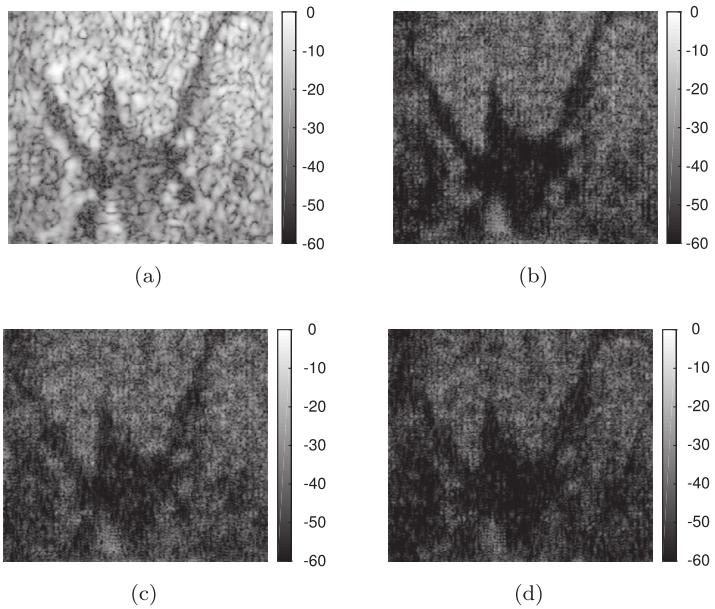

Fig. 3. Results on *in vivo* data. (a) Original US image, (b)–(d) reconstruction results using CSBD for CS ratios of 0.8, 0.6 and 0.4, obtained for $p = 1.5$.

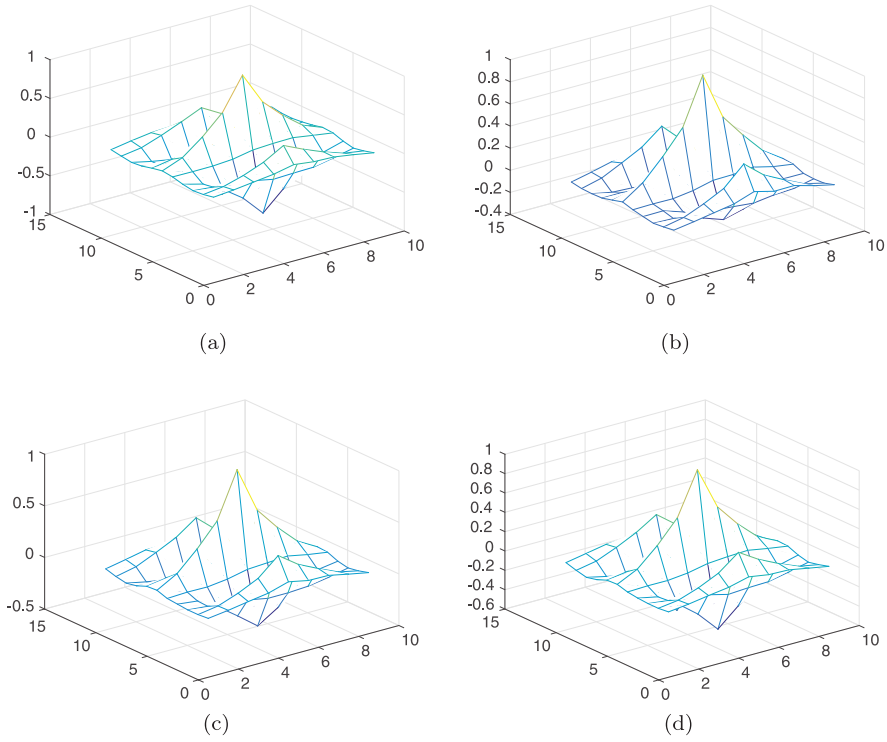

Fig. 4. Estimated PSFs with *in vivo* data. (a) Initial guess of PSF, (b)–(d) reconstruction results using CSBD for CS ratios of 0.8, 0.6 and 0.4.

initial guess of PSF. Moreover, the TRF reconstruction and PSF estimation of CSBD are very close to non-blind CD with the true PSF, which means that the algorithm converges to a critical point which may be close to the global minimizer in this case. We emphasize that CSBD is in fact an algorithm to a non-convex minimization problem, and the convergence largely depends on the hyperparameters. In this study, we manually tuned these hyperparameters including the number of iterations to get the best results. For this set of hyperparameters, the reconstruction took around 9 minutes for the simulated image and 5 minutes for the *in vivo* data on the MacBook Air with 2.2 GHz Intel Core i7 and 8 GB RAM.

With the *in vivo* data, in the absence of TRF and PSF ground truth thus avoiding the computation of quantitative metrics, we can visually appreciate the contrast improvement of TRF reconstructions in Fig. 3(c), (d) compared to the original US image in Fig. 3(a). We may also observe from Fig. 4 that the PSFs corresponding to the *in vivo* data do not follow a Gaussian shape

as we simulated in Fig. 2, especially in the axial direction. This is in fact a typical US PSF, shown as [36]. With a relatively good initial guess of the PSF in Fig. 4(a), our proposed CSBD method can preserve the shape and calibrate the accuracy of the PSF at the same time.

4. Conclusions

The main objective of this paper is to propose an algorithm dedicated to reconstruct enhanced ultrasound images from compressed measurements with an unknown PSF, namely compressive semi-blind deconvolution. Compared to the non-blind compressive deconvolution method, the proposed method can achieve better reconstructions on both TRF and PSF. In addition to more validations with experimental data, our future work will also include the consideration of the parametric model of US PSF, to incorporate the prior information on its shape. Moreover, some existing non-convex optimization techniques with convergence guarantee, such as coordinate descent, would be of great interest to this problem.

Conflict of interest statement

There is no conflict of interest for this article.

Appendix A

For the purpose of online PSF estimation, we write the convolution model as below [37]:

$$\boldsymbol{r} = XP\boldsymbol{h} + \boldsymbol{n} \tag{10}$$

where $\boldsymbol{r}, \boldsymbol{h}, \boldsymbol{n}$ are the observation, the PSF and the noise in vector forms respectively, $\boldsymbol{r}, \boldsymbol{n} \in \mathbb{R}^N$, $\boldsymbol{h} \in \mathbb{R}^n$. We should note that in practical situations the size of the PSF is much smaller than the image size, *i.e.* $n << N$. $X \in \mathbb{R}^{N\times N}$ is the BCCB matrix representing the original image $\boldsymbol{x}$ and $P \in \mathbb{R}^{N\times n}$ is a matrix defined to extend $\boldsymbol{h}$ to N. Let us denote the size of $\boldsymbol{x}$ and $H\boldsymbol{x}$ as $N = S \times T$, and the size of the PSF kernel $\boldsymbol{h}$ as $n = s \times t$.

X has exactly the same structure as H, classically used in deconvolution problems. The matrix P can be written as

$$P = \begin{bmatrix} P' \\ \bigcirc \end{bmatrix}$$

where $\bigcirc \in \mathbb{R}^{S(T-t)\times n}$ is a zero matrix and $P' \in \mathbb{R}^{St\times n}$ has the following structure

$$P' = \begin{bmatrix} I_s & \boldsymbol{O}_s & \dots & \boldsymbol{O}_s \\ \boldsymbol{O}_{(S-s)s} & \boldsymbol{O}_{(S-s)s} & \dots & \boldsymbol{O}_{(S-s)s} \\ \boldsymbol{O}_s & I_s & \dots & \boldsymbol{O}_s \\ \boldsymbol{O}_{(S-s)s} & \boldsymbol{O}_{(S-s)s} & \dots & \boldsymbol{O}_{(S-s)s} \\ \vdots & \vdots & \ddots & \vdots \\ \boldsymbol{O}_s & \boldsymbol{O}_s & \dots & I_s \\ \boldsymbol{O}_{(S-s)s} & \boldsymbol{O}_{(S-s)s} & \dots & \boldsymbol{O}_{(S-s)s} \end{bmatrix}$$

where $\boldsymbol{O}_s$ represents a zero square matrix of size $s \times s$ and $\boldsymbol{O}_{(S-s)s}$ is a zero matrix of size $(S-s) \times s$, I_s is an identity square matrix of size $s \times s$.

Appendix B

In Section 2, the analytical solution for PSF estimation is

$$\boldsymbol{h}^{k+1} = [(X^{k+1}P)^t X^{k+1} P + \gamma I_n]^{-1} (X^{k+1}P)^t \Psi\boldsymbol{a} \tag{11}$$

To simplify the notations, we will ignore the iteration number k and denote $\Psi\boldsymbol{a}$ by $\boldsymbol{z}$. The key to solve this equation is to find an efficient way to compute $(XP)^t XP$ and $(XP)^t\boldsymbol{z}$.

Firstly, for the term of $(XP)^t\boldsymbol{z}$, X^t is actually the BCCB matrix of the transformed $\boldsymbol{x}$. Let us denote the transformed $\boldsymbol{x}$ by $\boldsymbol{x}'$. $X^t\boldsymbol{z}$ is then the convolution between $\boldsymbol{x}'$ and $\boldsymbol{z}$. While $\boldsymbol{x}$ represents the 2D image $\boldsymbol{x}_{2D}$ in a vectorized version, $\boldsymbol{x}'$ corresponds to the transformed 2D image $\boldsymbol{x}'_{2D}$. We define the pixels of $\boldsymbol{x}$ in 2D by:

$$\boldsymbol{x}_{2D} = \begin{bmatrix} x_{11} & x_{12} & x_{13} & \dots & x_{1T} \\ x_{21} & x_{22} & x_{23} & \dots & x_{2T} \\ x_{31} & x_{32} & x_{33} & \dots & x_{3T} \\ \vdots & \vdots & \vdots & \ddots & \vdots \\ x_{S1} & x_{S2} & x_{S3} & \dots & x_{ST} \end{bmatrix}$$

The transformation from $\boldsymbol{x}_{2D}$ to $\boldsymbol{x}'_{2D}$ usually includes flips both in horizontal and vertical directions. However, the exact details of these flips depend also on the way the convolution product is defined, including its boundary conditions and the way the full convolution product is cropped to the size of the original image. Hereafter we will detail the transformation in the case of circular convolution with periodic boundary extensions, and we consider the center part of the full convolution. Thus $\boldsymbol{x}_{2D}$ can be obtained by flipping $\boldsymbol{x}$ twice: the first row to the last second and first column to the last second, which gives

$$\boldsymbol{x}'_{2D} = \begin{bmatrix} x_{(S-1)(T-1)} & x_{(S-1)(T-2)} & \dots & x_{(S-1)1} & x_{(S-1)T} \\ x_{(S-2)(T-1)} & x_{(S-2)(T-2)} & \dots & x_{(S-2)1} & x_{(S-2)T} \\ \vdots & \vdots & \ddots & \vdots & \vdots \\ x_{1(T-1)} & x_{1(T-2)} & \dots & x_{11} & x_{1T} \\ x_{S(T-1)} & x_{S(T-2)} & \dots & x_{S1} & x_{ST} \end{bmatrix}$$

According to the analysis on P above, P^t multiplying a vector is actually equivalent to choosing several elements from a vector. In our case, P^t aims picking up the first s elements from every S elements until we get n elements.

Secondly, concerning the term $P^t X^t XP$, its result is actually a matrix of size $n \times n$. To avoid constructing the big matrix P or X during implementation, we can find a way to compute these $n \times n$ elements instead.

Let us denote $U = X^t X$, U is a symmetric matrix following the structure:

$$U = \begin{bmatrix} U_1 & U_2 & U_3 & \dots & U_T \\ U_2 & U_1 & U_2 & \dots & U_{T-1} \\ U_3 & U_2 & U_1 & \dots & U_{T-2} \\ \vdots & \vdots & \vdots & \ddots & \vdots \\ U_T & U_{T-1} & U_{T-2} & \dots & U_1 \end{bmatrix}$$

where U_i $(i = 1, 2...T)$ is a matrix of size $S \times S$. Let us analyse the elements in this relative small matrix.

We know that every column in X is a transformed $\boldsymbol{x}$. This kind of transformation includes circulation both in horizontal

and vertical directions. Let us denote the image which is circulated i times in horizontal direction and j times in vertical direction as $\boldsymbol{x}_{2D}^{(ij)}$. Take an example, $\boldsymbol{x}_{2D}^{(12)}$ is equal to

$$x^{(12)} = \begin{bmatrix} x_{(S-1)T} & x_{(S-1)1} & x_{(S-1)2} & \dots & x_{(S-1)(T-1)} \\ x_{ST} & x_{S1} & x_{S2} & \dots & x_{S(T-1)} \\ x_{1T} & x_{11} & x_{12} & \dots & x_{1(T-1)} \\ \vdots & \vdots & \vdots & \ddots & \vdots \\ x_{(S-2)T} & x_{(S-2)1} & x_{(S-2)2} & \dots & x_{(S-2)(T-1)} \end{bmatrix}$$

As a result, every element in $X^t X$ is an inner product between two $\boldsymbol{x}^{(ij)}$ (vectorized image $\boldsymbol{x}_{2D}^{(ij)}$). Now we can present every detail of U_i. Here we use $\boldsymbol{x}^{(ij)}$ as the vectorized image.

$$U_i = \begin{bmatrix} \boldsymbol{x}^{(00)}\boldsymbol{x}^{(i0)} & \boldsymbol{x}^{(00)}\boldsymbol{x}^{(i1)} & \dots & \boldsymbol{x}^{(00)}\boldsymbol{x}^{(i(S-1))} \\ \boldsymbol{x}^{(01)}\boldsymbol{x}^{(i0)} & \boldsymbol{x}^{(01)}\boldsymbol{x}^{(i1)} & \dots & \boldsymbol{x}^{(01)}\boldsymbol{x}^{(i(S-1))} \\ \vdots & \vdots & \ddots & \vdots \\ \boldsymbol{x}^{(0(S-1))}\boldsymbol{x}^{(i0)} & \boldsymbol{x}^{(0(S-1))}\boldsymbol{x}^{(i1)} & \dots & \boldsymbol{x}^{(0(-1)S)}\boldsymbol{x}^{(i(S-1))} \end{bmatrix}$$

As we can see, U_i is also a symmetric matrix. Moreover, since $x^{00}x^{ij} = x^{00}x^{i(S-j)}$, there are several elements with the same values even in the same row.

After understanding every detail about the $X^t X$, now we can try to choose several elements out of the matrix to get the final result of $P^t X^t X P$. According to the definition of P we mentioned before, the structure of $P^t X^t X P$ can be written as

$$P^t X^t X P = \begin{bmatrix} U'_1 & U'_2 & U'_3 & \dots & U'_t \\ U'_2 & U'_1 & U'_2 & \dots & U'_{t-1} \\ U'_3 & U'_2 & U'_1 & \dots & U'_{t-2} \\ \vdots & \vdots & \vdots & \ddots & \vdots \\ U'_t & U'_{t-1} & U'_{t-2} & \dots & U'_1 \end{bmatrix}$$

where $U'_i \in \mathbb{R}^{s \times s}$ is

$$U'_i = \begin{bmatrix} x^{(00)}x^{(i0)} & x^{(00)}x^{(i1)} & \dots & x^{(00)}x^{(i(s-1))} \\ x^{(01)}x^{(i0)} & x^{(01)}x^{(i1)} & \dots & x^{(01)}x^{(i(s-1))} \\ \vdots & \vdots & \ddots & \vdots \\ x^{(0(s-1))}x^{(i0)} & x^{(0(s-1)}x^{(i1)} & \dots & x^{(0(s-1))}x^{(i(s-1))} \end{bmatrix}$$

In conclusion, an efficient way to solve $P^t X^t X P$ is to compute the $s \times s$ matrix U'_i. Since $P^t X^t X P$ is symmetric, we will need only to compute U'_i $(i = 1, 2, .., t)$. Moreover, for each and U'_i, only the calculations of $x^{00}x^{ij}$ $(j = 0, 1, ...s-1)$ are required, the computational cost is thus further reduced.

References

[1] Friboulet D, Liebgott H, Prost R. Compressive sensing for raw RF signals reconstruction in ultrasound. In: Ultrasonics symposium, IUS. IEEE; 2010. p. 367–70.

[2] Quinsac C, Basarab A, Girault J-M, Kouamé D. Compressed sensing of ultrasound images: sampling of spatial and frequency domains (regular paper). In: IEEE workshop on signal processing systems. IEEE; 2010. p. 231–6.

[3] Quinsac C, Basarab A, Gregoire J-M, Kouamé D. 3D compressed sensing ultrasound imaging (regular paper). In: IEEE international ultrasonic symposium. IEEE; 2010. p. 363–6.

[4] Achim A, Buxton B, Tzagkarakis G, Tsakalides P. Compressive sensing for ultrasound RF echoes using a-stable distributions. In: 2010 annual international conference of the IEEE engineering in medicine and biology society. IEEE; 2010.

[5] Chernyakova T, Eldar Y. Fourier-domain beamforming: the path to compressed ultrasound imaging. IEEE Trans Ultrason Ferroelectr Freq Control 2014;61(8):1252–67.

[6] Lorintiu O, Liebgott H, Alessandrini M, Bernard O, Friboulet D. Compressed sensing reconstruction of 3D ultrasound data using dictionary learning and line-wise subsampling. IEEE Trans Med Imaging 2015;34(12):2467–77.

[7] Jin KH, Han YS, Ye JC. Compressive dynamic aperture B-mode ultrasound imaging using annihilating filter-based low-rank interpolation. In: 2016 IEEE 13th international symposium on biomedical imaging; 2016. p. 1009–12.

[8] Besson A, Carrillo RE, Bernard O, Wiaux Y, Thiran JP. Compressed delay-and-sum beamforming for ultrafast ultrasound imaging. In: 2016 IEEE international conference on image processing; 2016. p. 2509–13.

[9] Liu J, He Q, Luo J. A compressed sensing strategy for synthetic transmit aperture ultrasound imaging. IEEE Trans Med Imaging 2017;36(4):878–91.

[10] Schiffner MF, Schmitz G. Fast compressive pulse-echo ultrasound imaging using random incident sound fields. J Acoust Soc Am 2017;141(5):3611.

[11] Liu J, He Q, Luo J. Compressed sensing based synthetic transmit aperture imaging: validation in a convex array configuration. IEEE Trans Ultrason Ferroelectr Freq Control 2017;PP(99):1. https://doi.org/10.1109/TUFFC.2017.2682180.

[12] Candès EJ, Wakin MB. An introduction to compressive sampling. IEEE Signal Process Mag 2008;25(2):21–30.

[13] Quinsac C, Basarab A, Kouamé D. Frequency domain compressive sampling for ultrasound imaging. Adv Acoust Vib, Adv Acoust Sens, Imag, Signal Process 2012;12:1–16. http://www.hindawi.com/journals/aav/2012/231317/.

[14] Schiffner MF, Schmitz G. Fast pulse-echo ultrasound imaging employing compressive sensing. In: 2011 IEEE international ultrasonics symposium. IEEE; 2011. p. 688–91.

[15] Liebgott H, Prost R, Friboulet D. Pre-beamformed RF signal reconstruction in medical ultrasound using compressive sensing. Ultrasonics 2013;53(2):525–33.

[16] Michailovich OV, Adam D. A novel approach to the 2-D blind deconvolution problem in medical ultrasound. IEEE Trans Med Imaging 2005;24(1):86–104.

[17] Jirik R, Taxt T. Two-dimensional blind Bayesian deconvolution of medical ultrasound images. IEEE Trans Ultrason Ferroelectr Freq Control 2008;55(10):2140–53.

[18] Zhao N, Basarab A, Kouamé D, Tourneret J-Y. Joint segmentation and deconvolution of ultrasound images using a hierarchical Bayesian model based on generalized Gaussian priors. IEEE Trans Image Process 2016;25(8):3736–50.

[19] Chen Z, Basarab A, Kouamé D. Compressive deconvolution in medical ultrasound imaging. IEEE Trans Med Imaging 2016;35(3):728–37.

[20] Ma J, Le Dimet F-X. Deblurring from highly incomplete measurements for remote sensing. IEEE Trans Geosci Remote Sens 2009;47(3):792–802.

[21] Xiao L, Shao J, Huang L, Wei Z. Compounded regularization and fast algorithm for compressive sensing deconvolution. In: 2011 sixth international conference on image and graphics. IEEE; 2011. p. 616–21.

[22] Zhao M, Saligrama V. On compressed blind de-convolution of filtered sparse processes. In: 2010 IEEE international conference on acoustics speech and signal processing. IEEE; 2010. p. 4038–41.

[23] Amizic B, Spinoulas L, Molina R, Katsaggelos AK. Compressive blind image deconvolution. IEEE Trans Image Process 2013;22(10):3994–4006.

[24] Bahmani S, Romberg J. Compressive deconvolution in random mask imaging. IEEE Trans Comput Imag 2015;1(4):236–46.

[25] Taxt T, Strand J. Two-dimensional noise-robust blind deconvolution of ultrasound images. IEEE Trans Ultrason Ferroelectr Freq Control 2001;48(4):861–6.

[26] Michailovich O, Tannenbaum A. Blind deconvolution of medical ultrasound images: a parametric inverse filtering approach. IEEE Trans Image Process 2007;16(12):3005–19.

[27] Chen Z, Basarab A, Kouamé D. Reconstruction of enhanced ultrasound images from compressed measurements using simultaneous direction method of multipliers. IEEE Trans Ultrason Ferroelectr Freq Control 2016;63(10):1525–34.

[28] Chen Z, Basarab A, Kouamé D. Enhanced ultrasound image reconstruction using a compressive blind deconvolution approach (regular paper). In: IEEE international conference on acoustics, speech, and signal processing. IEEE; 2017.

[29] Almeida MS, Almeida LB. Blind and semi-blind deblurring of natural images. IEEE Trans Image Process 2010;19(1):36–52.

[30] Yu C, Zhang C, Xie L. A blind deconvolution approach to ultrasound imaging. IEEE Trans Ultrason Ferroelectr Freq Control 2012;59(2):271–80.

[31] Morin R, Bidon S, Basarab A, Kouamé D. Semi-blind deconvolution for resolution enhancement in ultrasound imaging. In: 2013 20th IEEE international conference on image processing, ICIP. IEEE; 2013. p. 1413–7.

[32] Repetti A, Pham MQ, Duval L, Chouzenoux E, Pesquet J-C. Euclid in a taxicab: sparse blind deconvolution with smoothed regularization. IEEE Signal Process Lett 2015;22(5):539–43.

[33] Wang Y, Yang J, Yin W, Zhang Y. A new alternating minimization algorithm for total variation image reconstruction. SIAM J Imaging Sci 2008;1(3):248–72.é

[34] Do TT, Gan L, Nguyen NH, Tran TD. Fast and efficient compressive sensing using structurally random matrices. IEEE Trans Signal Process 2012;60(1):139–54.

[35] Wang Z, Bovik AC, Sheikh HR, Simoncelli EP. Image quality assessment: from error visibility to structural similarity. IEEE Trans Image Process 2004;13(4):600–12.

[36] Zhao N, Wei Q, Basarab A, Kouamé D, Tourneret J-Y. Blind deconvolution of medical ultrasound images using a parametric model for the point spread function (regular paper). In: IEEE international ultrasonics symposium. IEEE; 2016. p. 1–4.

[37] Morin R. Amélioration de la résolution en imagerie ultrasonore. Toulouse, France. PhD: Université de Toulouse; 2013. Thèse de doctorat, in French (November 2013).